A High Output Triboelectric–Electromagnetic Hybrid Generator Based on In-Phase Parallel Connection

Tiancong Zhao, Bo Niu, Guangci Xie, Chao Hu, Boying Liu, Minyi Xu,* and Yong Ma*

With the advent of carbon neutrality, renewable energy installations are being upgraded toward miniaturization, low cost, and high conversion efficiency. Thus, a high output triboelectric–electromagnetic hybrid generator based on in-phase parallel connection (IP-HG) is proposed. The output characteristics of both TENG (triboelectric nanogenerator) and EMG (electromagnetic generator) can be effectively complemented to provide excellent output over a wide range of operating frequencies. By connecting multiple TENGs in parallel with EMGs in the same phase respectively, cumbersome rectification elements and wiring can be eliminated, and the energy output of the device can be greatly increased. The output characteristics and advantages of the IP-HG are systematically investigated, including the material of the TENG, the rotation speed, the combination of dielectrode, and their effect on the electrical output of the IP-HG. The short-circuit current of 63 mA, open-circuit voltage of 80 V, and an instantaneous output power density of 610 W m^{-3} is obtained by using a full-wave rectifier circuit at 243 rpm, which can charge a 470 µF capacitor to 1 V in 0.2 s. A maximum output efficiency reaches 36.162% at 189 rpm. In addition, the IP-HG can continuously power a commercial sensor and three 5 W DC light bulbs at very low rotational speeds. The reported IP-HG offers an efficient and sustainable design approach to the development of hybrid harvesters.

1. Introduction

Natural resources give people a limited amount of energy to use, and as energy is constantly being used, the trend is toward the development and use of new energy sources.[1] The winds, ocean currents, and waves that exist in nature are

T. Zhao, B. Niu, G. Xie, B. Liu, Y. Ma
School of Marine Engineering and Technology
Sun Yat-Sen University
Guangzhou 510275, China
E-mail: mayong3@mail.sysu.edu.cn
T. Zhao, B. Niu, G. Xie, C. Hu, Y. Ma
Southern Marine Science and Engineering Guangdong Laboratory (Zhuhai)
Zhuhai 519000, China
M. Xu
Marine Engineering College
Dalian Maritime University
Dalian 116026, China
E-mail: xuminyi@dlmu.edu.cn

mobile energy sources and have great potential for development.[2–8] Currently, most energy harvesters use electromagnetic generator (EMG), which makes it difficult to harvest low frequency energy directly.[4,9,10] Triboelectric nanogenerator (TENG) uses an alternating electric field to generate an induced current by creating a polarized charge on the electrodes.[11–17] TENG has a high output voltage and can be matched to various types of commercial sensors.[5,10,18–27] Thus, TENG is well suited as a self-powered energy source for distributed devices, ensuring long battery life and real-time monitoring.[1,28–32] The rotating TENG is the most suitable device for harvesting energy because its voltage is largely independent of the rotational speed and the current is proportional to the rotational speed, which is a great advantage for powering external loads.[5,33–42] Lin et al.[36] designed a long-lived and robust rotating TENG that greatly reduces frictional losses, but has the disadvantage of low output. Bai et al.[33] proposed a TENG-based charge pump strategy with a peak power of 658 mW at a frequency of 2 Hz, but the prerequisite is that an external voltage source is required for pre-charging to excite the charge. Xu et al.[28] significantly enhanced the electrical output of TENG. By connecting the multiple parallel TENG units in-phase, the power density of the TENG increases proportionally with the number of the parallel unit. Zhao et al.[9] reviewed the study of ocean kinetic energy harvesters and concluded that HG (i.e. a combination of TENG and EMG) is a good choice for harvesting disordered, high entropy energy in the ocean.[43,44]

The TENGs are adapted to collect low frequency ambient energy, while EMGs are more suited to collect high frequency energy. On this basis, the hybrid generator combines the advantages of TENG (high voltage) and EMG (high current) with low cost, high resistance to complex environmental loads, high energy conversion efficiency, wide operating bandwidth, stable output characteristics. Guo et al.[45] combined the advantages of EMG and TENG and reported a hybrid generator for harvesting mechanical energy in harsh environments. Wang et al.[43] presented a hybridized triboelectric–electromagnetic water wave energy harvester in which the TENG utilizes the contact-free-standing mode. This work achieves mutual compensation of TENG and EMG, enabling the hybrid system to provide satisfactory output over a wide range of operating frequencies.

Feng et al.[46] designed a hybrid generator containing soft-contact cylindrical TENG and EMG with swing structure to achieve ultra-low frequency wave energy converting. The optimized hybrid generator exhibits the best output response at 0.1 Hz water wave agitation, delivering a peak power density of 10.16 W/m^3 and an average power density of 0.23 W m^{-3}. Lee et al.[16] manufactured a hybridized blue energy harvester based on pendulum design, containing an interdigital electrode-based TENG (I-TENG), a switch based TENG (S-TENG), and an EMG. The output power of the device can reach 5.11 W m^{-3} at a load of 100 Ω. Besides, the output and power density of hybrid generators with different work modes are provided in Table S1.

Herein we propose a high output triboelectric–electromagnetic hybrid generator based on in-phase parallel connection. The rotor of the TENG is fixed to the rotor of the EMG, and the upper and lower stators generate electrical energy by excitation of the external force. As the TENG and EMG play complementary roles in terms of output performance, the novel design can provide substantial power over a wide range of frequencies. In this work, the influence of the designed parameters, including the material optimization of the TENG and the electrical output characteristics when connected in parallel in the same phase, is systematically investigated experimentally. With the utilization of the in-phase parallel connection,

the IP-HG can increase its output by paralleling multiple units and is simple in structure and easy to package. This work represents a solid progress in improving the applications of the hybrid generator toward the sustainable power source for electronics.

2. Results and Discussion

2.1. Device Structure and Working Mechanism

The device structure of IP-HG is schematically shown in **Figure 1**a, which consists of two main parts: the stator and the rotor. The rotor rotates under the action of external force, which in turn generates electrical energy for the TENG and EMG. Figure 1b shows the internal structure and composition of the IP-HG. The stator consists of metal coils, an acrylic substrate, a PCB, metal electrodes, and a dielectric film. the stator of the EMG uses a side length of 200 mm, 15 mm thick acrylic plate as a substrate and embeds 9 coils. The stator of the TENG is adhered to the EMG stator and is covered with a dielectric film (50 μm thickness) before a complementary radially patterned copper electrode (18 segments) with a diameter of 150 mm was deposited on the PCB substrate. The metal electrode patterns of
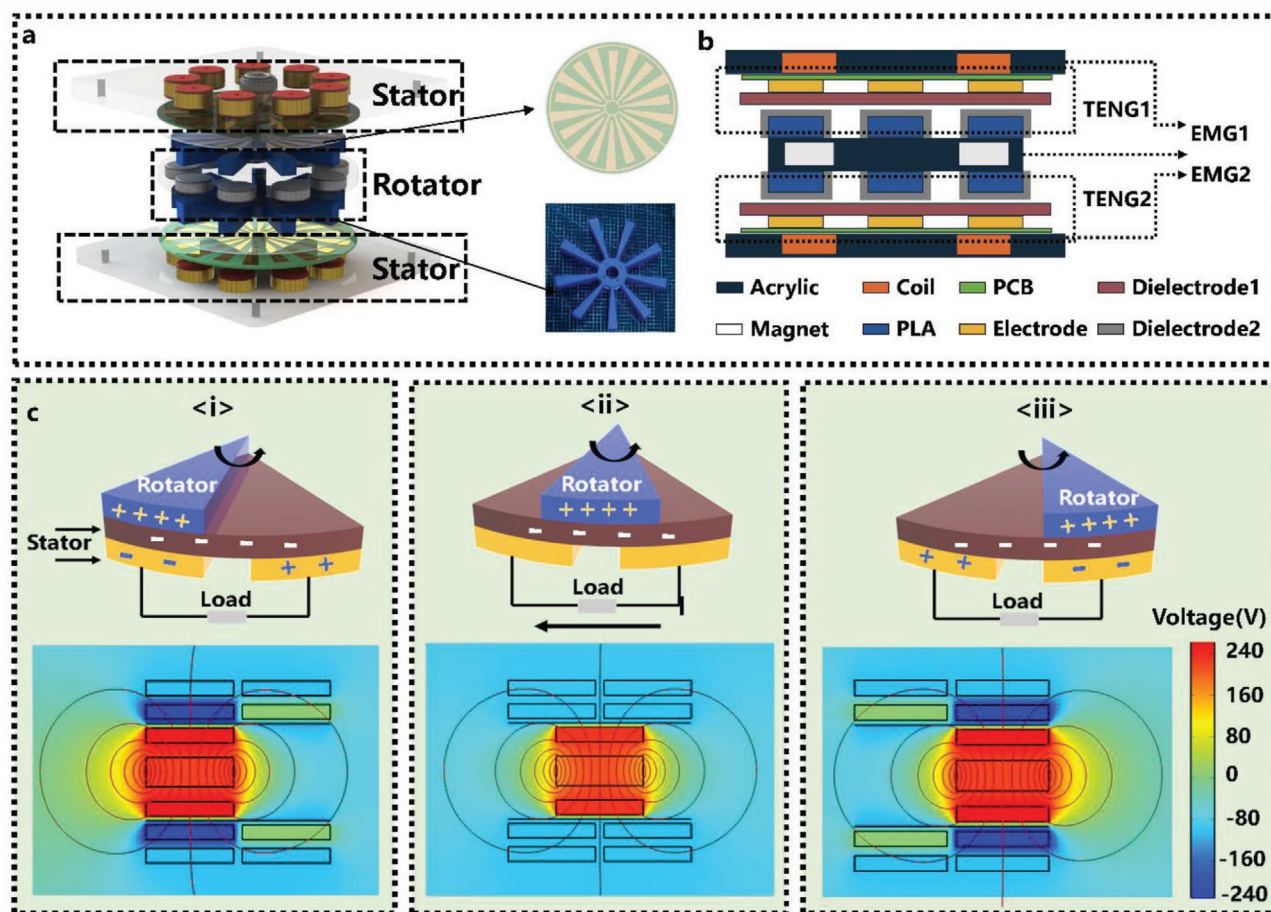

Figure 1. Structural design of the IP-HG. a) Schematic diagram of the designed hybridized generator, which mainly consists of two parts, two rotary radial electrode structure mode TENG units and two EMG units. b) Material composition of the IP-HG. c) Schematic diagram of the working mechanism of IP-HG.

**ADVANCED
SCIENCE NEWS**
www.advancedsciencenews.com

**ADVANCED
MATERIALS
TECHNOLOGIES**
www.advmattechnol.de

the upper and lower TENG stators are aligned with the output ports to ensure same-phase output. The rotor of the IP-HG consists of 3D printed PLA fan blades, acrylic substrate, and magnets. Two fan blades of nine TENGs (40° angle) prepared by the 3D printer are fixed by flange couplings on a circular acrylic plate with nine circular permanent magnets (diameter: 30 mm, thickness: 10 mm) embedded uniformly. The nine sector blades have the same cross-sectional pattern as the metal electrodes and correspond to each of the nine magnets. Due to the limited effective area of the acrylic rotor, the optimum number of magnets is arranged as nine, thus to correspond to this, the TENG rotor, the metal coil was also chosen as number 9 for the study. Increasing the above number within the limited range of the device increases the electron transfer frequency to increase the current output to ensure that the TENG and EMG triboelectric start and cut magnetic induction produce similar phases of current, which further allows the output power to be efficiently transferred to the consumer or stored via the energy management circuit. In order to ensure sufficient contact and friction, the fan blades have a soft sponge foam applied in the direction facing the stator as a cushioning layer and wrapped with a paper tape. The advantages of this structure are that the TENG and EMG can be connected in parallel in the same phase respectively. The output can be maximized by increasing the number of units. By combining the Triboelectric nanogenerator, TENG, and the Electromagnetic generator, EMG, the output characteristics of both can be effectively complemented to provide excellent output over a wide range of operating frequencies.

As shown in Figure 1c, the COMSOL Multiphysics software is utilized to simulate the schematic diagram of the current, charge distribution, magnetic flux, and potential distribution under short-circuit conditions to explain the mechanism of operation of the IP-HG. The rotor blades and magnets of the TENG were perfectly aligned with the coil in order to make the neat output of the TENG and EMG. During the rotation of the rotor, equal amounts of negative and positive electricity are generated on the FEP surface and the metal electrode surface respectively due to the different electron affinities between the metal electrode and the FEP. In the initial state <i>, the negative and positive charges are induced at the left and right electrodes respectively due to electrostatic induction to shield the electric field. Then during the rotation <ii>, a potential difference is generated between the electrodes, and the negative charge on the left electrode is transferred to the right electrode via an external circuit to maintain the equilibrium state until the final state <iii> is reached. Due to the symmetrical structure of the disc, an opposite potential difference is induced in the next cycle, so that the current flows in the opposite direction. The simulation cloud shows that the rotating TENG open-circuit voltage can theoretically reach 240 V. At the same time, the magnetic flux through the coil decreases as the rotor of the EMG rotates from its initial state to its final state. By Lenz's law this causes the current in the coil to generate a magnetic field and prevents the flux from decreasing and thus generating a current.[45]

2.2. The Output and Characteristics of IP-HG

In order to test and verify the simulation results, we built the IP-HG experimental test rig and shown in **Figure 2**a. The overall test rig is arranged vertically and is composed of bearings, torque transducers, couplings, adjustable speed motors, 3D printed standoffs, and an optical stage. Available TENG materials are first tested to find the effect of material combinations on TENG output performance. For a TENG, the open-circuit voltage and short circuit current can be expressed as:[45]

$$V_{oc}^{TE} = \frac{\sigma S}{C} \tag{1}$$

$$I_{SC}^{TE} = \frac{n}{\pi} \frac{\sigma}{2} S\omega \tag{2}$$

As shown in Figure 2b, five different combinations of materials were selected for comparison. The materials selected were the more common materials available on the market. Copper and gold for the materials of metal electrodes deposited on the PCB. The surface materials of the rotor blades were chosen from masking tapes and nylon cloth. Besides, the dielectric materials were chosen from PTFE (Poly tetra fluoroethylene) and FEP (Fluorinated ethylene propylene). Interestingly, we found that at a speed of 81 rpm, a single TENG made of Au-FEP-Masking tape could achieve an open-circuit voltage V_{oc}^{TE} of 230 V, a short-circuit current I_{SC}^{TE} of 5.1 µA, a transferred charge Q of 82 nC, and a peak output power P_{max} of 1.173 mW.

However, the V_{oc}^{TE}, I_{SC}^{TE}, Q and P_{max} of a conventional Cu-PTFE-Nylon single TENG are 60 V, 1.4 µA, 25 nC, and 0.084 mW respectively. This shows that we have found a cost-effective and low-cost combination of materials at a low speed, with a single TENG unit delivering 14 times more power than the original combination. As shown in Figure 2f–h, V_{oc}^{TE} is 390 V, I_{SC}^{TE} is 21 µA and Q is 150 nC. A clear waveform plot of the nine cycles is given in Figure S2, Supporting Information. We have further tested the data with multiple TENGs connected in parallel in the same phase without rectification, and the output performance has the desired superposition effect, as explained in detail in our original work.[28]

In **Figure 3**, the TENG theoretical model can be modeled as a capacitor in series with the TENG in the diagram. Experimentally we found that a higher number of cells connected in parallel in the same phase gives a higher voltage output, a phenomenon that we have explained in previous work. We consider the equivalent capacitance value of the electrostatic meter to be much greater than that of the TENG. However, this explanation has limitations and ignores the effect of the increase in equivalent capacitance value when the TENG is connected in parallel. It is worth pointing out that the voltage values obtained from the test here are smaller than the actual values because the electrostatic meter contains a capacitance of 0.3 nF, which is measured by means of a multimeter capacitance class. The actual voltage value divides most of the electrical energy to charge the equivalent capacitor in the electrostatic meter, resulting in a small test voltage value. The voltage value we measure is closely related to the equivalent capacitance value of the electrostatic meter. As shown in Figure 3a, assuming $C_{T1}=C_{T2} = C_{Tn}$, $Q_{sc,1} = Q_{sc,2} = Q_{sc,n}$, we can get:
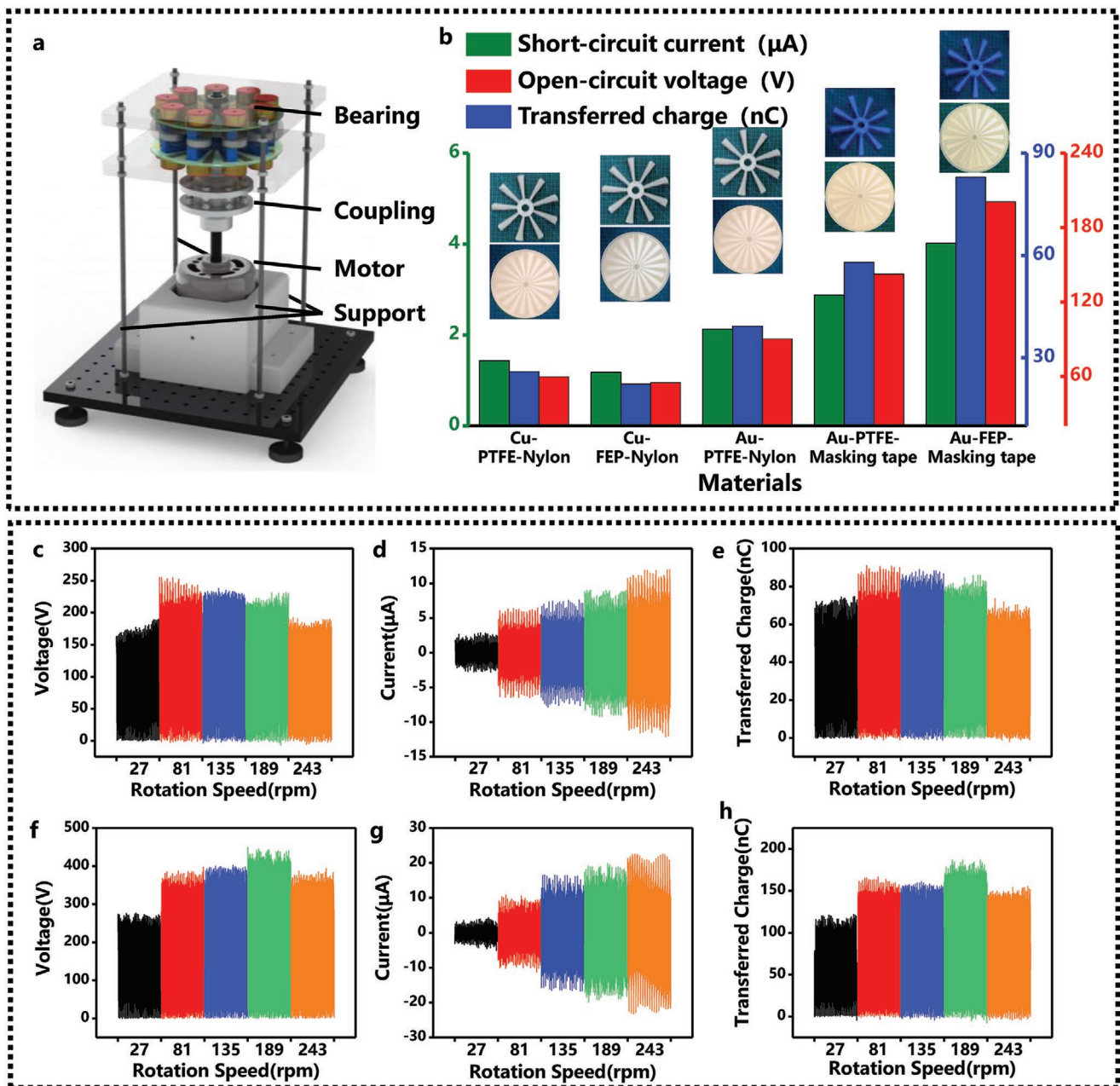
**ADVANCED
SCIENCE NEWS**

www.advancedsciencenews.com

**ADVANCED
MATERIALS
TECHNOLOGIES**

www.advmattechnol.de

Figure 2. Materials and units that influence the electric output of TENG. a) Photograph of the experiment platform for IP-HG. b) Open-circuit voltage, short-circuit current, and transferred charges of the TENGs fabricated with different dielectric materials. c) V_{oc}, d) I_{sc}, e) Q_{sc} of single TENG. f) V_{oc}, g) I_{sc}, h) Q_{sc} of double TENG in parallel.

$$V_s = \frac{nQ_{sc}}{nC_T + C_v} \tag{3}$$

$$V_f = \frac{Q_{sc}}{C_T} \tag{4}$$

In Equations (3) and (4), V_s is the voltage value of the n-layer generation unit measured by the electrostatic meter, the V_f is the voltage value of the actual *n*-layer generation unit when connected in parallel in the same phase. Thus,

$$V_f = V_s \cdot \left(1 + \frac{C_v}{nC_T}\right) \tag{5}$$

Substituting the parameters of this paper into Equation (5),

$$\frac{V_f}{V_s} = 4.4 \frac{1}{n} + 1 \tag{6}$$

V_f is actually a constant value depending on the material or structural properties of the TENG, and as more units are added

**ADVANCED
SCIENCE NEWS**
www.advancedsciencenews.com

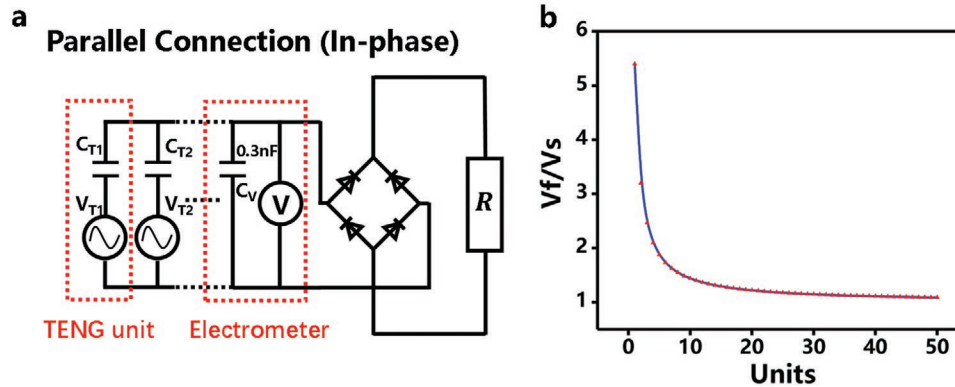**ADVANCED
MATERIALS
TECHNOLOGIES**
www.advmattechnol.de

Figure 3. Relationship between actual and tested values of voltage. a) The equivalent circuit diagram of a TENG and b) the relationship between the number of in-phase parallel units and V_f/V_s.

the effect of the equivalent capacitance of the electrostatic meter on the actual voltage value measured is actually being reduced. As we can see from Figure 3b, when 50 units are connected in parallel in the same phase, the actual test voltage is almost equal to the meter test voltage. In fact, we can see from the diagram that by connecting 10 units in parallel, most of the lost power can be extracted. In practice, energy management circuits, sensors, or appliances all have equivalent capacitance, which corresponds to Equation (6) in a different way, so we can use increasing the number of units to improve the energy utilization of the device.

2.3. Energy Output Capability of IP-HG

In Figure S1, Supporting Information, we note that at low speeds the EMG can only provide a very low voltage and cannot be used to power electronic devices; in contrast, the TENG can always maintain a high voltage and can be used as a transient power source. this characteristic of the TENG would be advantageous for harvesting low frequency mechanical energy, which is more common in the environment. We know that the characteristics of the TENG and EMG are very different: at constant speed, the TENG can be seen as a current source with a large output resistance, while the EMG is equivalent to a voltage source with a small internal resistance.

According to previous work, an ideal voltage source and an ideal current source can be connected in parallel, with the TENG being considered a current source and the EMG being used as a voltage source. Therefore, when the TENG and EMG are rectified separately and connected in parallel they should exhibit the characteristics of a voltage source. Furthermore, in conventional linear power circuits due to the Davinan equivalent and Norton equivalent, the voltage at the ends of a parallel circuit consisting of a voltage source and a current source is determined by the voltage source, while the current magnitude of the load circuit is determined by U/R and has no relationship with the magnitude of the current source. However, through experiments, we found that the equivalent circuit schematic of a single TENG and EMG rectified and connected in parallel respectively, as shown in **Figure 4**a, presents a different phenomenon from the theory in the experimental DC Figure 4b

and voltage Figure 4c. The current is 0.3 mA and the voltage is 2.9 V when the IP-HG is rotating at 27 rpm. We find that the current increases rapidly with increasing speed and at 243 rpm the current and voltage of the IP-HG reach 26 mA and 38 V respectively. Figure 4d shows the equivalent circuit schematic of two sets of TENG and EMG connected in parallel in the same phase and then rectified separately and then connected in parallel. Experimental tests show that the current is 3.8 mA and 27 V at a low speed of 27 rpm and 61 mA and 80 V at 243 rpm and remains constant at subsequent speeds (Figure 4e,f). This shows that when the TENG and EMG are connected in parallel and in phase, the output maintains the high current output performance of the EMG and the high voltage characteristics of the TENG.

To further verify this, we have tested the power load characteristics of two TENGs in parallel in phase, two EMGs in parallel in phase, and the above two rectified groups in parallel, as shown in Figure 4g–i, as well as the ability to charge capacitors. At a fixed speed of 135 rpm, Figure 4g(i) shows the maximum output power of 5.4 mW for two TENGs connected in parallel in phase at a load resistance of 90 MΩ, 7.89 mW for two EMGs connected in parallel in phase at a load resistance of 24 Ω in Figure 4h(i), and 8.31 mW for the IP-HG at a load resistance of 30 Ω in Figure 4I(i). This shows that the IP-HG still follows the output characteristics of a voltage source and that by connecting several TENGs in parallel in the same phase arrangement. Theoretically, when a current source is connected in parallel with a voltage source, the load characteristics will take on the characteristics of a voltage source, as the internal resistance of the current source is infinite and can be considered as a broken circuit, so the load characteristics of a compound generator are closer to those of an EMG. In addition, we believe that the voltage values increase when connected in parallel because the voltage waveforms of the TENG and EMG are superimposed after rectification. The reason for the instability of the superimposed voltage values at a low speed of 27 rpm is that the voltage amplitude of the EMG at low frequencies, the generation frequency differs significantly from that of the TENG, so that an unstable pulse is formed, corresponding to this phenomenon when the speed is increased decreases. Figure 4f shows the voltage output is 70 times higher than that of the EMG and is more stable at high speeds. At 243 rpm, the IP-HG can achieve an instantaneous output power
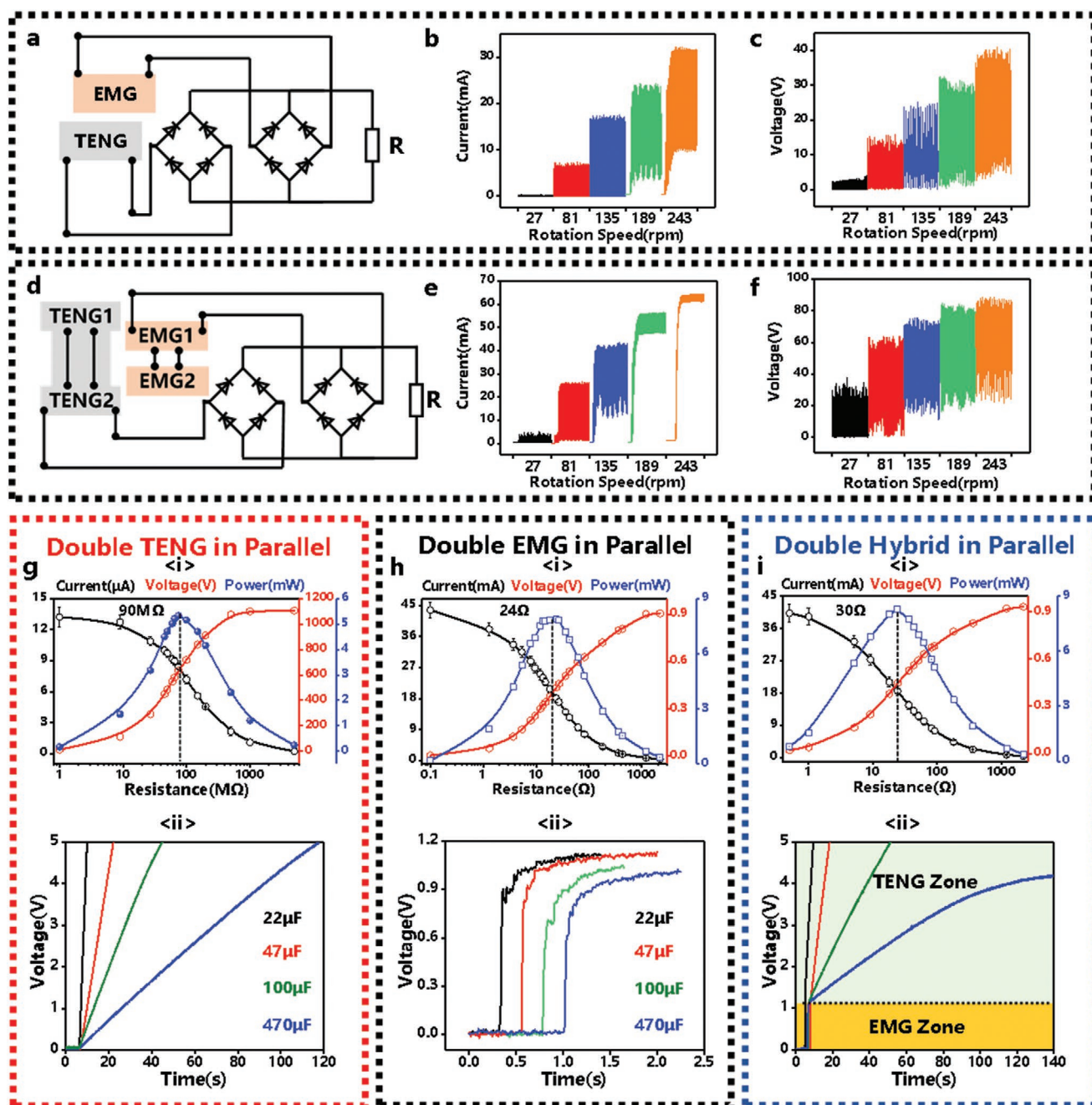
**ADVANCED
SCIENCE NEWS**

www.advancedsciencenews.com

**ADVANCED
MATERIALS
TECHNOLOGIES**

www.advmattechnol.de

Figure 4. The energy output performances of IP-HG. a) Schematic diagram of the equivalent circuit for a single TENG and EMG rectified separately and connected in parallel and the output performance of direct current (b) and voltage (c). d) Schematic diagram of an equivalent circuit with two sets of TENG and EMG in parallel in the same phase and then rectified separately and then connected in parallel and the output performance of the DC current (e) and voltage (f). g) Power characteristic curves <i> of two TENGs connected in parallel and then rectified at different resistances and <ii> the ability to charge different capacitors. h) Power characteristic curves <i> of two EMGs connected in parallel and then rectified at different resistances and <ii> the ability to charge different capacitors. i) Power characteristic curves <i> and the ability <ii> to charge different capacitors for two sets of TENG, EMG respectively connected in parallel and then rectified and then connected in parallel at different resistances.

density of 610 W m^{-3}, which is a new breakthrough in the field of hybrid generator. Thus, the IP-HG has a high voltage and high current output and the output performance can be increased by connecting more TENGs and EMGs in parallel in the same phase arrangement. Figure 4g–i(ii) then shows the ability of the different energy harvesting devices to charge the capacitor, with

the TENG being able to charge a 470 µF capacitor to 5 V in 120 s and the EMG being able to charge a 470 µF capacitor to 1 V in 0.2 s, but not to a higher voltage due to the small voltage. The IP-HG inherits the advantages of both the TENG and the EMG, maintaining a constant rate of energy supply to the capacitor even after a rapid charge to 1 V.
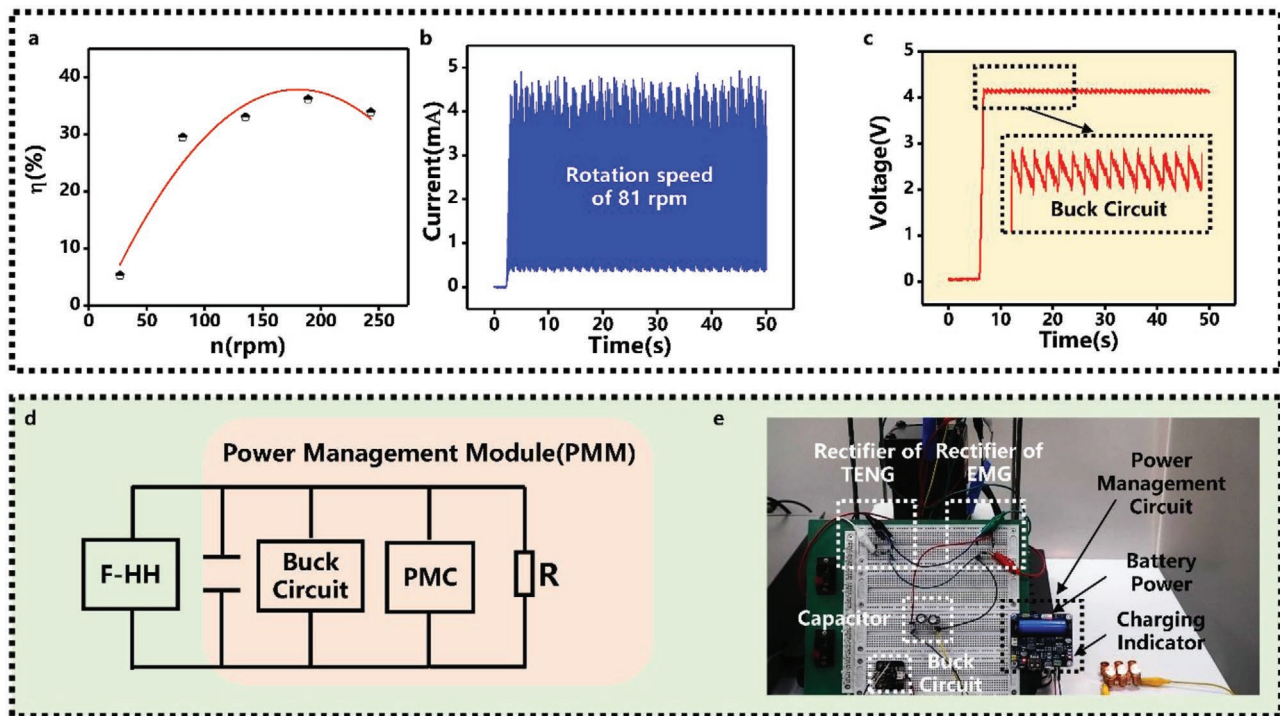
**ADVANCED
SCIENCE NEWS**

www.advancedsciencenews.com

**ADVANCED
MATERIALS
TECHNOLOGIES**

www.advmattechnol.de

Figure 5. The demonstration of IP-HG. a) The efficiency for the IP-HG. The stable IP-HG current (b) and voltage (c) through buck circuit. d) IP-HG with power management module (PMM) and e) to keep lighting of 3 DC bulbs of 5 W in series.

2.4. The Demonstration of IP-HG

In order to consider the effective performance of the device, the efficiency for the IP-HG is given by:

$$\eta = \frac{P_{out}}{P_{in}} = \frac{UI}{M\omega} \tag{7}$$

Here, P_{out} and P_{in} is the output of electrical energy and the input of mechanical energy, respectively. U is the load voltage, I is the load current, M is the torque, ω is the angular speed. Torque M measured by dynamic torque sensor (CYT-303 Micro Range Torque Transducer) is 0.6 Nm. **Figure 5**a shows that the two units have a maximum output efficiency of 36.162% at 189 rpm. The existing shortcomings are that the number of units can be increased to 10 and that a structure with less starting torque can be used between the rotor and the stator, which in turn allows more power to be captured. Further optimizations and improvements will be made in subsequent work.

In addition, as shown in Figure S3, Supporting Information, at a fixed speed of 81 rpm for the IP-HG, a 22 μF capacitor discharge can continuously supply the temperature sensor. To make the signal output from the IP-HG more stable, we adopt a hybrid circuit which consists of a full-bridge rectifier circuit, a filter capacitor, a step-down circuit, and an energy management circuit. The rectifier bridge is used to convert the AC output of the hybrid generator into a DC output. Buck circuit for filtering and reducing DC pulsations. In the energy management circuit, we use maximum power point tracking (MPPT), a system that regulates the operation of electrical modules so

that the power generator can output more power and store the DC power efficiently in the battery. Figure 5b,c shows that at 81 rpm the average current is 2.5 mA and the voltage is stable at 4.2 V. To make efficient use of this power, the output of the buck circuit is further optimized using an energy management circuit. In Figure 5 d,e and Movie S1, Supporting Information, the output of the buck circuit can always power the battery in the energy management circuit, charging a Li battery to 20% in 5 min and lighting up three 5 W DC bulbs.

3. Conclusion

In summary, we have demonstrated a high output triboelectric–electromagnetic hybrid generator based on in-phase parallel connection (IP-HG). By creatively using multiple TENGs in parallel with EMGs in the same phase the cumbersome wiring of the rectifier can be eliminated and the energy output of the device can be greatly increased. The effect of the designed parameters, including the material of the TENG, the rotation speed, and the type of combination, on the electrical output of the IP-HG was systematically investigated through experiments. Compared to conventional EMGs, the IP-HG is able to generate stable voltages and continuously power commercial sensors even at very low rotational speeds. The IP-HG obtains a mixed output of 63 mA short-circuit current, 80 V open-circuit voltage at 243 rpm, an instantaneous output power density of 610 W m^{-3}, which can charge a 470 μF capacitor to 1 V in 0.2 s. Finally, the IP-HG was shown to be able to directly power three 5 W DC lamps by using an energy management module. This novel design is perfectly suited to the continuous operation of

commercially available sensors. And it is simple, cost-effective, and easy to package and provide a design idea for the hybrid harvesters.

4. Experimental Section

Fabrication of the TENG Part: TENG consists of a stator and a rotor. The copper electrode layer (thickness 30 µm) has complementary sectors (18 sectors in total) with the same center angle of about 10°, which were coated on the substrate by means of PCB technology. For the stator, a layer of FEP film (thickness 50 µm) is adhered to face the rotor for insulation purposes. For the rotor, nine fan blades (10 mm thick, diameter of 150 mm) were machined using a 3D printer with the same pattern as one of the electrodes and corresponding to the metal electrodes and magnets. The fan blades were glued with soft foam in the direction facing the stator to act as a cushioning layer and wrapped with a paper tape to act as a friction layer for each blade.

Fabrication of an EMG: Manufacturing of EMG: EMG also consists of two parts: stator and rotor. For the stator, an acrylic plate with a side length of 200 mm and a thickness of 15 mm was used as the substrate. On one side of the substrate, 9 circular slots with a depth of 15 mm were cut and 9 coils (275 turns each, wire diameter of 0.5 mm) were embedded. For the rotor, 9 NdFeB permanent magnets of 30 mm diameter and 10 mm thickness were aligned with the TENG rotor blades and fixed on an acrylic plate of 160 mm diameter and 10 mm thickness. To reduce the resistance between the parts, bearings were used to connect the rotor of the TENG, the stator of the EMG, and the rotor.

Assembling of the IP-HG: The rotor of the TENG is fixed to the rotor of the EMG by means of a flange coupling (30 mm outer diameter, 10 mm inner diameter). the stator of the TENG is glued to the acrylic substrate of the EMG.

Electrical Measurement: For the purpose of performance evaluation, the open-circuit voltage and short-circuit current of the TENG device were measured by a Keithley 6514 system electrometer. The software platform was constructed based on LabVIEW, which was capable of realizing real-time data acquisition control and analysis. The simulation system of the speed-controlled motor (US-52) equipped with a reduction gearbox (5GN-5K). The reduction ratio of speed-controlled motor is 5. The speed adjustment is achieved by selecting different gears. When the first gear is selected, the motor input speed is 135 r min^{-1}, so the reducer output speed is 27 r min^{-1}; when the third gear is selected, the motor input speed is 405 r min^{-1}, so the reducer output speed is 81 r min^{-1}; when the fifth gear is selected, the motor input speed is 675 r min^{-1}, so the reducer output speed is 135 r min^{-1}. Torque M measured by dynamic torque sensor (CYT-303 Micro Range Torque Transducer). Finally, the buck circuit and power management circuit (MPPT) of the IP-HG was used for powering three 5 W DC bulbs in series.

Supporting Information

Supporting Information is available from the Wiley Online Library or from the author.

Conflict of Interest

The authors declare no conflict of interest.

Data Availability Statement

The data that support the findings of this study are available from the corresponding author upon reasonable request.

[1] Z. L. Wang, *Nano Energy* **2018**, *54*, 477.
[2] Q. Schiermeier, J. Tollefson, T. Scully, *Nature* **2008**, *454*, 816.
[3] J. Tollefson, *Nature* **2014**, *508*, 302.
[4] Z. L. Wang, T. Jiang, L. Xu, *Nano Energy* **2017**, *39*, 9.
[5] T. Jiang, H. Pang, J. An, P. Lu, Y. Feng, X. Liang, W. Zhong, Z. L. Wang, *Adv. Energy Mater.* **2020**, *10*, 2000064.
[6] S. H. Salter, *Nature* **1974**, *249*, 720.
[7] J. Scruggs, P. Jacob, *Science* **2009**, *323*, 1176.
[8] Z. L. Wang, *Nature* **2017**, *542*, 159.
[9] T. Zhao, M. Xu, X. Xiao, Y. Ma, Z. Li, Z. L. Wang, *Nano Energy* **2021**, *88*, 106199.
[10] J. An, Z. M. Wang, T. Jiang, X. Liang, Z. L. Wang, *Adv. Funct. Mater.* **2019**, *29*, 1904867.
[11] Z. L. Wang, *ACS Nano* **2013**, *7*, 9533.
[12] X. Wang, S. Niu, Y. Yin, F. Yi, Z. You, Z. L. Wang, *Adv. Energy Mater.* **2015**, *5*, 1501467.
[13] M. Xu, P. Wang, Y.-C. Wang, S. L. Zhang, A. C. Wang, C. Zhang, Z. Wang, X. Pan, Z. L. Wang, *Adv. Energy Mater.* **2018**, *8*, 1702432.
[14] B. Shi, Z. Li, Y. Fan, *Adv. Mater.* **2018**, *30*, 1801511.
[15] Z. L. Wang, *Mater. Today* **2017**, *20*, 74.
[16] L. Liu, Q. Shi, C. Lee, *Nano Energy* **2020**, *76*, 105052.
[17] Y. Wang, X. Liu, T. Chen, H. Wang, C. Zhu, H. Yu, L. Song, X. Pan, J. Mi, C. Lee, M. Xu, *Nano Energy* **2021**, *90*, 106503.
[18] X. Li, J. Tao, X. Wang, J. Zhu, C. Pan, Z. L. Wang, *Adv. Energy Mater.* **2018**, *8*, 1800705.
[19] G. Liu, H. Guo, S. Xu, C. Hu, Z. L. Wang, *Adv. Energy Mater.* **2019**, *9*, 1900801.
[20] X. Zhang, M. Yu, Z. Ma, H. Ouyang, Y. Zou, S. L. Zhang, H. Niu, X. Pan, M. Xu, Z. Li, Z. L. Wang, *Adv. Funct. Mater.* **2019**, *29*, 1900327.
[21] X. Liang, T. Jiang, Y. Feng, P. Lu, J. An, Z. L. Wang, *Adv. Energy Mater.* **2020**, *10*, 2002123.
[22] X. Xiao, X. Zhang, S. Wang, H. Ouyang, P. Chen, L. Song, H. Yuan, Y. Ji, P. Wang, Z. Li, M. Xu, Z. L. Wang, *Adv. Energy Mater.* **2019**, *9*, 1902460.
[23] Y. C. Lai, Y. C. Hsiao, H. M. Wu, Z. L. Wang, *Adv. Sci.* **2019**, *6*, 1801883.
[24] X. Zhang, M. Yu, Z. Ma, H. Ouyang, Y. Zou, S. L. Zhang, H. Niu, X. Pan, M. Xu, Z. Li, Z. L. Wang, *Adv. Funct. Mater.* **2019**, *29*, 1900327.
[25] P. Jiang, L. Zhang, H. Guo, C. Chen, C. Wu, S. Zhang, Z. L. Wang, *Adv. Mater.* **2019**, *31*, 1902793.
[26] Z. H. Lin, G. Cheng, S. Lee, K. C. Pradel, Z. L. Wang, *Adv. Mater.* **2014**, *26*, 4690.
[27] Y. Wang, D. Liu, Z. Hu, T. Chen, Z. Zhang, H. Wang, T. Du, S. L. Zhang, Z. Zhao, T. Zhou, M. Xu, *Adv. Mater. Technol.* **2021**, *6*, 2001270.
[28] M. Xu, T. Zhao, C. Wang, S. L. Zhang, Z. Li, X. Pan, Z. L. Wang, *ACS Nano* **2019**, *13*, 1932.

[29] H. Zhao, X. Xiao, P. Xu, T. Zhao, L. Song, X. Pan, J. Mi, M. Xu, Z. L. Wang, *Adv. Energy Mater.* **2019**, *9*, 1902824.

[30] H. Wang, Z. Fan, T. Zhao, J. Dong, S. Wang, Y. Wang, X. Xiao, C. Liu, X. Pan, Y. Zhao, M. Xu, *Nano Energy* **2021**, *84*, 105920.

[31] H. Zhang, Y. Yang, Y. Su, J. Chen, K. Adams, S. Lee, C. Hu, Z. L. Wang, *Adv. Funct. Mater.* **2014**, *24*, 1401.

[32] Y. Wang, X. Liu, Y. Wang, H. Wang, H. Wang, S. L. Zhang, T. Zhao, M. Xu, Z. L. Wang, *ACS Nano* **2021**, *15*, 15700.

[33] Y. Bai, L. Xu, S. Lin, J. Luo, H. Qin, K. Han, Z. L. Wang, *Adv. Energy Mater.* **2020**, *10*, 2000605.

[34] J. Chen, H. Guo, C. Hu, Z. L. Wang, *Adv. Energy Mater.* **2020**, *10*, 2000886.

[35] L. Gao, S. Lu, W. Xie, X. Chen, L. Wu, T. Wang, A. Wang, C. Yue, D. Tong, W. Lei, H. Yu, X. He, X. Mu, Z. L. Wang, Y. Yang, *Nano Energy* **2020**, *72*, 104684.

[36] Z. Lin, B. Zhang, H. Zou, Z. Wu, H. Guo, Y. Zhang, J. Yang, Z. L. Wang, *Nano Energy* **2020**, *68*, 104378.

[37] P. Chen, J. An, R. Cheng, S. Shu, A. Berbille, T. Jiang, Z. L. Wang, *Energy Environ. Sci.* **2021**, *14*, 4523.

[38] P. Chen, J. An, S. Shu, R. Cheng, J. Nie, T. Jiang, Z. L. Wang, *Adv. Energy Mater.* **2021**, *11*, 2003066.

[39] L. Jin, S. L. Zhang, S. Xu, H. Guo, W. Yang, Z. L. Wang, *Adv. Mater. Technol.* **2021**, *6*, 2000918.

[40] P. Lu, H. Pang, J. Ren, Y. Feng, J. An, X. Liang, T. Jiang, Z. L. Wang, *Adv. Mater. Technol.* **2021**, *6*, 2100496.

[41] S. Yong, J. Wang, L. Yang, H. Wang, H. Luo, R. Liao, Z. L. Wang, *Adv. Energy Mater.* **2021**, *11*, 2101194.

[42] C. Zhang, Y. Liu, B. Zhang, O. Yang, W. Yuan, L. He, X. Wei, J. Wang, Z. L. Wang, *ACS Energy Lett.* **2021**, *6*, 1490.

[43] J. Wang, L. Pan, H. Guo, B. Zhang, R. Zhang, Z. Wu, C. Wu, L. Yang, R. Liao, Z. L. Wang, *Adv. Energy Mater.* **2019**, *9*, 1802892.

[44] C. Wu, A. C. Wang, W. Ding, H. Guo, Z. L. Wang, *Adv. Energy Mater.* **2019**, *9*, 1802906.

[45] H. Guo, Z. Wen, Y. Zi, M.-H. Yeh, J. Wang, L. Zhu, C. Hu, Z. L. Wang, *Adv. Energy Mater.* **2016**, *6*, 1501593.

[46] Y. Feng, X. Liang, J. An, T. Jiang, Z. L. Wang, *Nano Energy* **2021**, *81*, 105625.